

# Spreading Dynamics of Polymer Nanodroplets

David R. Heine, Gary S. Grest, and Edmund B. Webb III  
*Sandia National Laboratories, Albuquerque, New Mexico 87185*

(Dated: September 25, 2018)

The spreading of polymer droplets is studied using molecular dynamics simulations. To study the dynamics of both the precursor foot and the bulk droplet, large drops of 200,000 monomers are simulated using a bead-spring model for polymers of chain length 10, 20, and 40 monomers per chain. We compare spreading on flat and atomistic surfaces, chain length effects, and different applications of the Langevin and dissipative particle dynamics thermostats. We find diffusive behavior for the precursor foot and good agreement with the molecular kinetic model of droplet spreading using both flat and atomistic surfaces. Despite the large system size and long simulation time relative to previous simulations, we find no evidence of hydrodynamic behavior in the spreading droplet.

PACS numbers: 68.47.Pe

## I. INTRODUCTION

The spreading of liquid droplets on a surface is an important issue for several industries including adhesion, lubrication, coating, and printing. Emerging nanotechnology in areas such as lithography and microfluidics has made the issue of droplet spreading on small length scales even more relevant. Experiments on droplet spreading have revealed several phenomena involved in the spreading process, some of which occur on the atomic level and others that become relevant at mesoscopic length scales [1, 2, 3, 4, 5, 6, 7, 8, 9, 10, 11, 12, 13, 14, 15]. These include the spreading of a precursor foot ahead of the droplet [3], terraced spreading of mono-molecular layers [4, 16, 17], and viscous losses due to rolling motion [1, 18].

Several models have been proposed to describe the spontaneous spreading of liquid droplets on a surface. These models can be classified as molecular kinetic models, continuum hydrodynamic models, or combined models. The molecular kinetic theory of Eyring [19] has been applied to the kinetics of wetting by Blake and Haynes [20, 21] as well as Cherry and Holmes [22]. This theory treats the surface adsorption of liquid molecules as the dominant factor in the spreading of a droplet. The hydrodynamic theory [1, 2, 23, 24] focuses on the energy dissipation due to viscous flow in the droplet. It has been claimed that hydrodynamic dissipation is dominant for small contact angles and non-hydrodynamic dissipation is dominant for relatively large contact angles [25]. Since both mechanisms are present in spreading droplets, several groups have proposed combined theories [3, 8, 23, 26, 27, 28]. Experimental results for the spreading of poly(dimethylsiloxane) (PDMS) drops on bare silicon wafers have shown good agreement with one combined model [10].

The study of droplet spreading using molecular dynamics simulation has been hindered due to computational limitations restricting simulations to small droplet sizes and short times. Molecular dynamics simulations were first used to study the spreading of monomer and dimer liquids [29, 30, 31, 32]. However, the spreading of monomer and dimer droplets are clearly influenced by

the volatility of the small molecules, allowing them to vaporize and condense independent of the dynamics of the droplet. To separate the spreading from the vaporization and condensation, subsequent simulations used short bead-spring chain molecules since they have a very low vapor pressure. In most cases, the simulations reproduced the experimentally observed  $R \sim t^{1/2}$  scaling of the contact radius of the precursor foot on both atomistic [11, 33, 34, 35] and flat [36, 37] surfaces, though logarithmic scaling has also been observed [35]. It is believed that this difference is due to the corrugation of the substrate, producing  $t^{1/2}$  scaling for a sufficiently small lattice dimension and a logarithmic scaling for large, i.e. strong corrugation [38]. Milchev and Binder [39] have studied wetting using Monte Carlo simulations on a flat substrate which suggest Tanner's spreading law for the growth dynamics of the droplet holds on the nanoscopic scale. Other comparisons to theoretical models have strongly supported the molecular kinetic theory of wetting [40, 41, 42, 43, 44], probably due to the relatively small droplet sizes and short simulation times employed.

In this paper, we present results from extensive molecular dynamics simulations of coarse-grained models of polymer droplets wetting a surface. Although most recent simulations of droplet spreading use droplets containing 20,000 to 32,000 monomers [11, 33, 34, 35, 40, 42], we consider drops composed of 100,000 to 200,000 monomers to simultaneously study the precursor foot and bulk regions for long times. We compare simulations performed using both a flat surface and an atomistic substrate to determine if the computationally expensive atomistic substrate is required to obtain correct spreading dynamics. We also evaluate different implementations of the Langevin and dissipative particle dynamics (DPD) thermostats for efficiency and realism in preserving hydrodynamic effects. Also, the difference in using a spherical droplet as the starting configuration as opposed to a hemispherical droplet is discussed. We find that the method which captures all of the physics of the spreading drop in the most computationally efficient manner is to simulate large drops on flat substrates with a coupling to the thermostat which falls off exponentially with distance

from the substrate [45]. For atomistic substrates, we find coupling only the substrate monomers to the Langevin thermostat significantly more efficient than coupling the DPD thermostat to all monomers.

The paper is organized as follows. Section II describes the details of the molecular dynamics simulations and the application of the thermostats. Section III presents the results for the time dependence of the contact radius. The contact angle data is fit to models of droplet spreading in Section IV and conclusions are presented in Section V.

## II. SIMULATION DETAILS

### A. System

We perform molecular dynamics (MD) simulations using a coarse-grained model for the polymer chains in which the polymer is represented by spherical beads of mass  $m$  attached by springs. We use a cutoff Lennard-Jones (LJ) potential to describe the interaction between all monomers. The LJ potential is given by

$$U_{LJ}^{\alpha\beta}(R) = \begin{cases} 4\varepsilon_{\alpha\beta} \left[ \left( \frac{\sigma_{\alpha\beta}}{r} \right)^{12} - \left( \frac{\sigma_{\alpha\beta}}{r} \right)^6 \right] & r \leq r_c \\ 0 & r > r_c \end{cases} \quad (1)$$

where  $\varepsilon_{\alpha\beta}$  and  $\sigma_{\alpha\beta}$  are the LJ units of energy and length and the cutoff is set to  $r_c = 2.5 \sigma_{\alpha\beta}$ . We denote the polymer monomers as type 1 and substrate monomers as type 2. The monomer-monomer interaction,  $\varepsilon_{11} = \varepsilon$ , is used as the reference and all monomers have the same diameter  $\sigma_{\alpha\beta} = \sigma$ . For bonded monomers, we apply an additional potential where each bond is described by the finite extensible nonlinear elastic (FENE) potential [46],

$$U_{FENE}(r) = \begin{cases} \frac{-k}{2} R_0^2 \ln \left[ 1 - \left( \frac{r}{R_0} \right)^2 \right] & r \leq R_0 \\ \infty & r > R_0 \end{cases}, \quad (2)$$

with  $k = 30 \varepsilon$  and  $R_0 = 1.5 \sigma$ .

Droplets consisting of chains of length  $N = 10, 20$ , or 40 monomers per chain are created by first equilibrating a melt of the polymer and then removing molecules whose centers are outside of a hemisphere of a given radius,  $38 \sigma$  for non-wetting droplets and  $48 \sigma$  for wetting droplets. The droplet is then placed on either an atomistic substrate or a flat substrate.

The atomistic substrate is composed of LJ particles forming four layers of the (111) surface of an fcc lattice where the bottom layer is frozen and the top three layers maintain their structure through a strong LJ interaction,  $\varepsilon_{22} = 5\varepsilon$ . The masses of the substrate monomers are set to  $m_2 = 2m_1 = 2m$ . For non-wetting droplets, each layer of the substrate contains 12 000 monomers and the dimensions of the substrate are  $110.0\sigma \times 115.4\sigma$ . For

the wetting droplets, we study two substrates, containing either 49 200 or 99 960 monomers per layer. The dimensions of the substrates are  $231.2 \sigma \times 231.0 \sigma$  and  $330.8 \sigma \times 331.4 \sigma$ , respectively. We refer to these as the small, medium and large substrates. The large substrates are necessary because the finite size of the atomistic substrates require the use of periodic boundary conditions at their edges whereas the flat surface can extend indefinitely in the  $x$  and  $y$  directions. For the atomistic substrate, during the course of the simulation, the precursor foot reaches the edge of the substrate and interacts with the periodic image of the droplet. Although this can be related to the spreading of an array of nanodroplets, such as in micro-contact printing, we do not include any data for the precursor foot once it reaches the periodic image. The droplets consist of  $\sim 100,000$  monomers for non-wetting droplets and  $\sim 200,000$  monomers for wetting droplets. All simulations are run at a temperature of  $T = 1.0 \varepsilon/k_B$ .

For the flat surface, the interaction between the monomers in the droplet and the surface is modeled by an integrated LJ potential,

$$U_{LJ}^{wall}(z) = \begin{cases} \frac{2\pi\varepsilon_w}{3} \left[ \frac{2}{15} \left( \frac{\sigma}{z} \right)^9 - \left( \frac{\sigma}{z} \right)^3 \right] & z \leq z_c \\ 0 & z > z_c \end{cases} \quad (3)$$

with  $z_c = 2.2\sigma$ .

The equations of motion are integrated using a velocity-Verlet algorithm. We use a time step of  $\Delta t = 0.009 \tau$  where  $\tau = \sigma \left( \frac{m}{\varepsilon} \right)^{1/2}$ . The simulations are performed using the LAMMPS code [47] on 36 to 100 Dec Alpha processors of Sandia's *CPlant* cluster. Simulating one million steps for a wetting drop of 200,000 monomers on the medium atomistic substrate takes between 90 and 250 hours on 64 processors, depending on the thermostat.

### B. Thermostats

The choice of thermostat employed can greatly affect the droplet spreading dynamics, so we compare simulations that use the Langevin [48] and DPD [49, 50] thermostats. The purpose is to find an approach that is both computationally efficient and provides a realistic representation of the transfer of energy in the spreading droplet.

The Langevin thermostat simulates a heat bath by adding Gaussian white noise and friction terms to the equation of motion,

$$m_i \ddot{\mathbf{r}}_i = -\Delta U_i - m_i \gamma_L \dot{\mathbf{r}}_i + \mathbf{W}_i(t), \quad (4)$$

where  $\gamma_L$  is the friction parameter for the Langevin thermostat,  $-\Delta U_i$  is the force acting on monomer  $i$  due to the potentials defined above, and  $\mathbf{W}_i(t)$  is a Gaussian

white noise term such that

$$\langle \mathbf{W}_i(t) \cdot \mathbf{W}_j(t') \rangle = 6k_B T m_i \gamma_L \delta_{ij} \delta(t - t'). \quad (5)$$

The Langevin thermostat can either be coupled to all monomers in the system or just to those in the substrate. The advantage of the latter is that the long-range hydrodynamic interactions are preserved in the droplet, whereas coupling all monomers to the Langevin thermostat screens the hydrodynamic interactions. Both approaches are applied in the simulations to test the various models for droplet spreading discussed below in Sec. IV. The damping constant is chosen to be  $\gamma_L = 0.1 \tau^{-1}$  in most cases, which is much smaller than that arising from collisions between monomers.

Our next approach is to apply the thermostat from the DPD simulation method. The DPD technique includes a dissipative force term in the equations of motion along with random forces. The equation of motion for the DPD thermostat is

$$m_i \ddot{\mathbf{r}}_i = \sum_{j \neq i} (-\Delta U_{ij} + \mathbf{F}_{ij}^D + \mathbf{F}_{ij}^R). \quad (6)$$

In Eq. 6,  $\mathbf{F}_{ij}^D$  and  $\mathbf{F}_{ij}^R$  are the dissipative and random terms given by

$$\mathbf{F}_{ij}^D = -m_i \gamma_{DPD} w^2(r_{ij}) (\hat{\mathbf{r}}_{ij} \cdot (\dot{\mathbf{r}}_i - \dot{\mathbf{r}}_j)) \hat{\mathbf{r}}_{ij} \quad (7)$$

$$\mathbf{F}_{ij}^R = m_i \sigma_{DPD} w(r_{ij}) \zeta_{ij} \hat{\mathbf{r}}_{ij} \quad (8)$$

where  $\gamma_{DPD}$  is the DPD friction parameter,  $\sigma_{DPD}^2 = 2k_B T \gamma_{DPD}$ ,  $\zeta_{ij}$  is a Gaussian noise term with  $\langle \zeta_{ij}(t) \zeta_{kl}(t') \rangle = (\delta_{ik} \delta_{jl} + \delta_{il} \delta_{jk}) \delta(t - t')$ ,  $\mathbf{r}_{ij} = \mathbf{r}_i - \mathbf{r}_j$ ,  $r_{ij} = |\mathbf{r}_{ij}|$ , and  $\hat{\mathbf{r}}_{ij} = \mathbf{r}_{ij}/r_{ij}$ . The weight function  $w(r_{ij})$  is defined as

$$w(r_{ij}) = \begin{cases} (1 - r_{ij}/r'_c) & r_{ij} < r'_c \\ 0 & r_{ij} \geq r'_c. \end{cases} \quad (9)$$

We take  $r'_c = r_c = 2.5 \sigma$ . The advantage of this thermostatting technique is that the momentum is conserved locally and long-range hydrodynamic interactions are preserved even in the case where all monomers are coupled to the thermostat. All simulations with the DPD thermostat use  $\gamma_{DPD} = 0.1 \tau^{-1}$ , so the dissipation from the thermostat is much less than from monomer collisions as seen in Sec. IV. Simulations that use DPD couple the thermostat to all atoms in the system.

In the case of the flat substrate, we study several methods to thermostat the system. In the first, we simply couple the Langevin or DPD thermostat to all monomers. However this is somewhat unphysical since monomers near the substrate are expected to have a

stronger damping than those in the bulk of the droplet. In the case of the Langevin thermostat, this coupling of all monomers also means that the hydrodynamic interactions are screened. In addition, chains which separate from the droplet move across the substrate very rapidly, particularly for the DPD thermostat. For this reason, we did not further pursue the DPD thermostat on the flat substrate. To overcome these difficulties, we follow the approach of Braun and Peynard [45] and add an external Langevin coupling with a damping rate that decreases exponentially away from the substrate. We choose the form

$$\gamma_L(z) = \gamma_L^s \exp(\sigma - z) \quad (10)$$

where  $\gamma_L^s$  is the surface Langevin coupling and  $z$  is the distance from the substrate. We choose values of  $\gamma_L^s = 1.0, 3.0$ , and  $10.0 \tau^{-1}$ . There is no obvious a priori way to define the appropriate value of  $\gamma_L^s$ . However, one way is to choose  $\gamma_L^s$  so that the diffusion constant of the precursor foot is comparable for the flat and atomic substrates for comparable departures from the wetting/non-wetting transition (see Fig. 4 below).

### III. SIMULATION RESULTS

A droplet containing about 200,000 monomers for a wetting droplet is large enough to allow us to simultaneously study the bulk and precursor foot regions. This can be seen in the profile views for chain length  $N = 10$  in Figs. 1 and 2, which show the foot extending beyond the bulk region for wetting droplets on an atomistic substrate and a flat surface, respectively. Note that Fig. 1 shows the thickness of the foot increasing after it reaches the periodic image. The same behavior is seen when periodic boundaries are applied to the flat surface, so this is not an effect of the corrugation of the substrate.

To characterize the spreading dynamics of these droplets, we extract the instantaneous contact radius and contact angle every 10,000 to 40,000  $\Delta t$ . The contact radius is calculated by defining a two-dimensional radial distribution function,  $g(r) = \rho(r)/\rho$ , based on every particle within  $1.5 \sigma$  of the surface. The local density at a distance  $r$  from the center of mass of the droplet is

$$\rho(r) = \frac{N(r)}{2\pi r \Delta r} \quad (11)$$

where  $N(r)$  is the number of particles at a distance between  $r$  and  $r + \Delta r$  from the center of mass and  $\rho$  is the integral of  $\rho(r)$  over the entire surface. The contact radius is defined as the distance  $r$  at which  $g(r) = 0.98$ . This approach provides a robust measure of the radius at any point during the spreading simulation. The same calculation is used to obtain the droplet radius for ten slices of the droplet at incremental heights every  $1.5 \sigma$  from the surface. A line is fit to the resulting points and

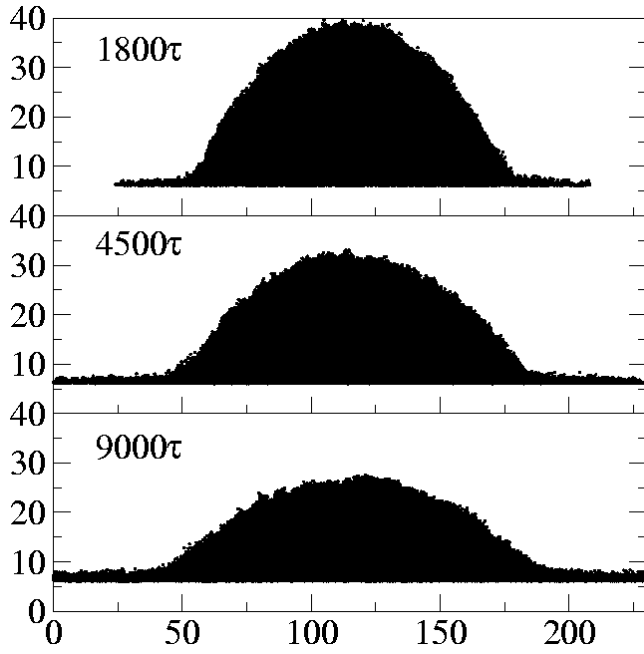


FIG. 1: Profile of the  $N = 10$  polymer droplet spreading on the atomistic substrate at three different times using the Langevin thermostat applied only to the substrate monomers with  $\gamma_L = 0.1 \tau^{-1}$  and  $\varepsilon_{12} = 1.5 \varepsilon$ .

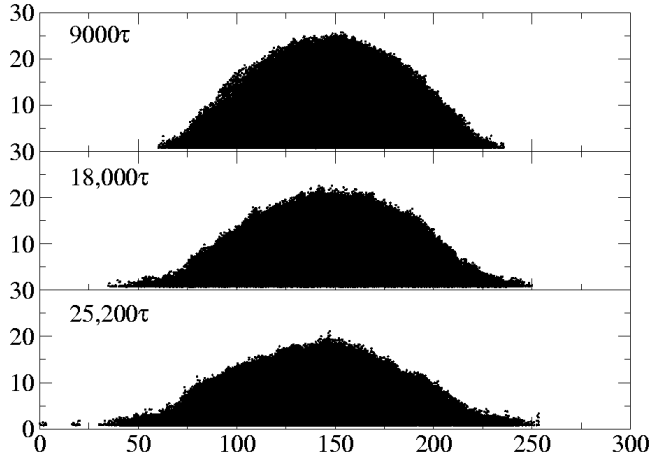


FIG. 2: Profile of the  $N = 10$  polymer droplet spreading on the flat surface at three different times using the surface Langevin thermostat.  $\gamma_L^s = 10.0 \tau^{-1}$ ,  $\varepsilon_w = 2.0 \varepsilon$ .

the instantaneous contact angle is determined from the slope of the line. For simulations that exhibit a precursor foot, the particles within  $4.5 \sigma$  of the surface are ignored in the contact angle calculation.

The non-wetting droplets reach their equilibrium configurations fairly rapidly, as shown by the contact angle data in Fig. 3. The equilibrium contact angle measured as a function of polymer-surface interaction strength is shown in Fig. 4. From this figure, it is clear that the transition from non-wetting to wetting occurs near  $\varepsilon_{12}^c \simeq 1.05 \varepsilon$  for droplets on a substrate and  $\varepsilon_w^c \simeq 1.75 \varepsilon$

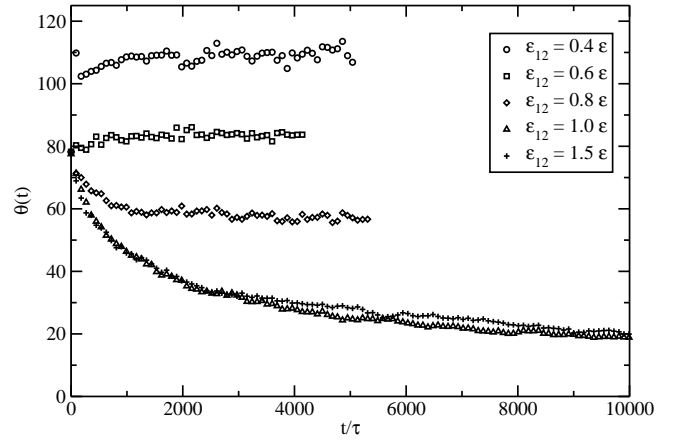


FIG. 3: Contact angle of non-wetting droplets of  $N = 10$  polymers on an atomistic substrate starting from a hemispherical

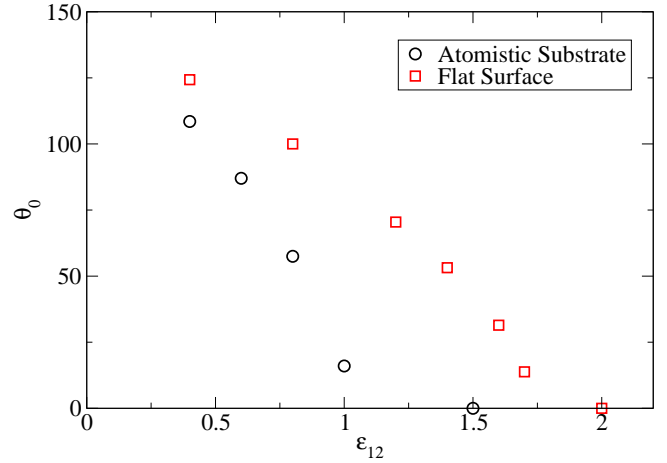


FIG. 4: Equilibrium contact angle as a function of polymer-surface interaction strength showing the transition from non-wetting to wetting for  $N = 10$  polymer droplets on an atomistic substrate (circles) and a flat surface (squares).

for droplets on a flat surface. For most of the wetting simulations, we use  $\varepsilon_{12} = 1.5 \varepsilon$  for the atomistic substrate and  $\varepsilon_w = 2.0 \varepsilon$  for the flat substrate, both well within the wetting regime.

The time dependence of the contact radius of the precursor foot and bulk region is shown in Fig. 5 for wetting droplets on an atomistic substrate for three chain lengths. The  $t^{1/2}$  behavior is evident for the precursor foot at all chain sizes, while the kinetics of the main droplet is clearly significantly slower. The  $N = 10$  data shown in Fig. 5 is taken from simulations on both the large and medium substrates whereas the  $N = 20$  and  $N = 40$  simulations are on the medium substrate. The contact radius of the bulk droplet increases steadily for all three chain lengths on the medium substrate. However, the run on the large substrate shows a slowing down and eventual contraction of the bulk contact radius as the foot con-

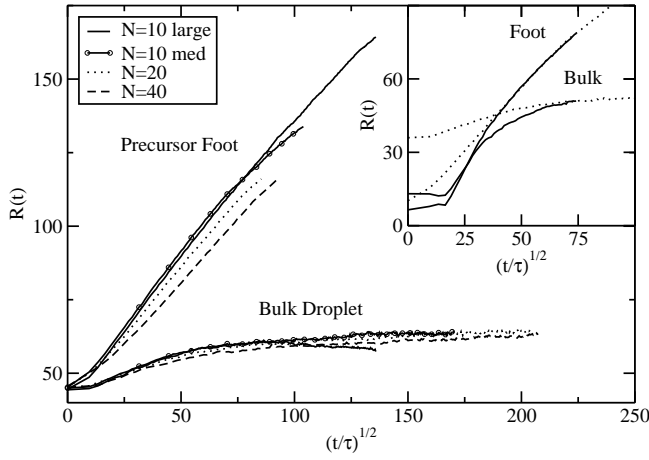


FIG. 5: Time dependence of the contact radius of the precursor foot and bulk droplet for wetting droplets on an atomistic substrate at three different chain lengths starting from a hemisphere with a contact angle of approximately  $90^\circ$ . The Langevin thermostat,  $\gamma_L = 0.1 \tau^{-1}$ , is applied only to the substrate monomers and  $\varepsilon_{12} = 1.5 \varepsilon$ . Results for  $N = 10$  are for both the medium and large atomistic substrates, while those for  $N = 20$  and  $40$  are for the medium atomistic substrate. The inset shows the contact radius for  $N = 10$  starting with a spherical droplet (solid line) compared to a hemispherical droplet (dotted). Results for the hemisphere in the inset have been shifted downward to easily compare the late time behavior.

continues outward, depleting the supply of material in the bulk faster than the drop can transfer material downward. This suggests that for our largest substrate, the drop size must be even larger to be able to study both the precursor foot and bulk droplet in the same simulation.

The inset in Fig. 5 shows the spreading of a spherical  $N = 10$  droplet compared to an initial hemisphere. The sphere is placed just above the substrate with zero initial velocity to avoid any effect due to impact velocity. The difficulty in measuring the spreading rate for this case is evident as it takes roughly  $1200 \tau$  for the sphere to adopt a hemispherical shape,  $1600 \tau$  for the spreading rate of the foot to match that of the hemisphere, and  $5000 \tau$  for the spreading rate of the bulk to match that of the hemisphere. (The hemisphere data for the foot and bulk regions are shifted downward to easily compare the spreading rates.)

Voué *et al.* [6, 11] found both experimentally for PDMS droplets and in numerical computer simulations that the diffusion constant of the precursor foot varies non-monotonically with increasing coupling to the substrate. At first, increasing the coupling to the substrate increases the driving force and the fluid spreads on the substrate more rapidly. However, further increases in the strength of the fluid substrate coupling, while increasing the driving force, also increase the friction of the fluid monomers with the substrate, resulting in a decrease in the diffusion constant. From the time dependence of  $R(t)$ , the diffusion constant  $D_f$  for the foot can

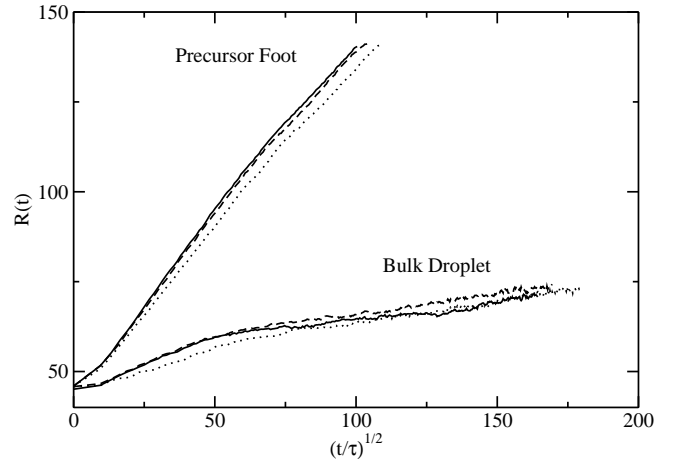


FIG. 6: Effect of thermostat on contact radius of precursor foot and bulk region for wetting droplets of  $N = 10$  polymers on an atomistic substrate for  $\varepsilon_{12} = 1.5 \varepsilon$ . The thermostats applied are DPD (solid line), Langevin on all monomers (dotted) and Langevin on only substrate monomers (dashed).  $\gamma_{DPD} = \gamma_L = 0.1 \tau^{-1}$ .

be determined from

$$\langle (R(t) - R(0))^2 \rangle = 4D_f t \quad (12)$$

The resulting diffusion constants are  $D_f = 0.34 \sigma^2/\tau$ ,  $0.30 \sigma^2/\tau$ , and  $0.23 \sigma^2/\tau$  for  $N = 10, 20$ , and  $40$  respectively for  $\varepsilon_{12} = 1.5 \varepsilon$ , indicating a very weak dependence on chain length, at least for these unentangled chains. Increasing  $\varepsilon_{12}$  to  $2.0 \varepsilon$ , we find  $D_f = 0.16 \sigma^2/\tau$  for  $N = 10$ , thus the droplets are in the high friction regime for these values of fluid substrate coupling.

Figure 6 shows the time dependence of the contact radius for wetting droplets on an atomistic substrate using different thermostatting techniques. These results show that there is essentially no difference in the spreading rate between the DPD thermostat applied to all monomers and the Langevin thermostat applied only to the substrate. We can see that applying the Langevin thermostat to all monomers slightly decreases the spreading rate as the viscous heating is removed from the system, though the resulting loss of hydrodynamic flow, at least for the droplet size studied here, has no significant impact.

For wetting droplets on a flat surface, the thermostat dependence of the contact radius is shown in Fig. 7. Here, the Langevin thermostat is applied either to all monomers (curves labeled with  $\gamma_L$ ) or with the surface Langevin coupling (curves labeled with  $\gamma_L^s$ ). The value of  $\gamma_L$  clearly has a strong influence on the spreading rate.  $\gamma_L^s = 3.0 \tau^{-1}$  gives a diffusion constant comparable to the atomistic substrate with  $\gamma_L = 0.1 \tau^{-1}$ . The chain length dependence of the contact radius is shown in Fig. 8. Again, the  $t^{1/2}$  behavior is evident in the foot region but not the bulk region. The chain length dependence on the flat surface is similar to the atomistic substrate,

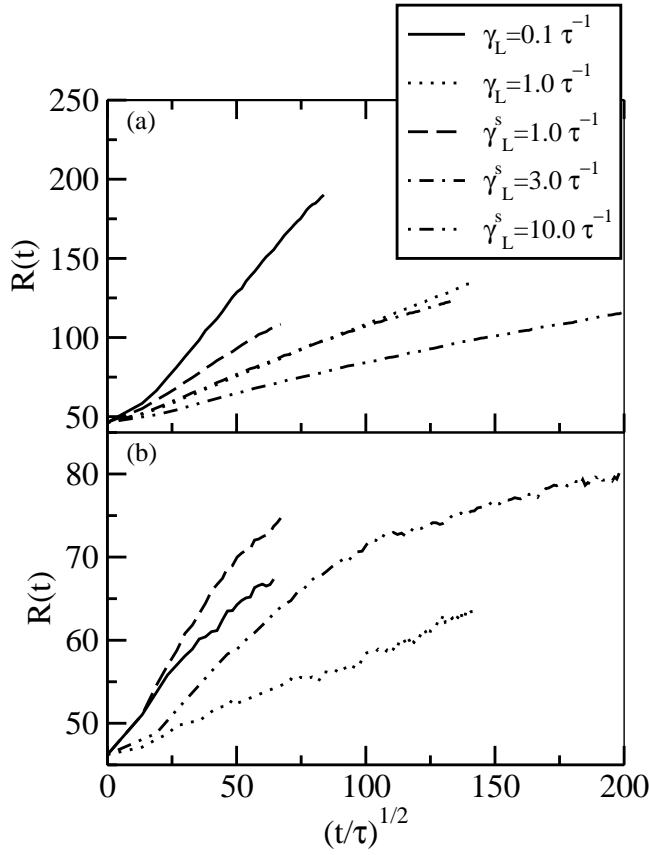


FIG. 7: Effect of thermostat on contact radius of (a) precursor foot and (b) bulk region for wetting droplets of  $N = 10$  polymers on a flat surface with  $\varepsilon_w = 2.0 \varepsilon$ .

showing a moderate decrease in spreading rate for larger polymers.

#### IV. MODELS OF DROPLET SPREADING DYNAMICS

##### A. Overview of models

The dynamics of droplet spreading are controlled by the driving force (the difference in surface tension  $\gamma$  at each interface) and by the energy dissipation. The total energy dissipation can be represented by a sum of three different components,  $T(\dot{\Sigma}_w + \dot{\Sigma}_f + \dot{\Sigma}_l)$  [3]. The first term,  $T\dot{\Sigma}_w$ , represents energy dissipation due to the hydrodynamic flow in the bulk of the droplet as more material is transferred to the surface.  $T\dot{\Sigma}_f$  relates to the viscous dissipation in the precursor foot present in cases of complete wetting. The third term,  $T\dot{\Sigma}_l$ , refers to the dissipation in the vicinity of the contact line due to the adsorption and desorption of liquid molecules to the solid surface. Here, we compare models that incorporate one or more of these dissipation mechanisms to our simulation results.

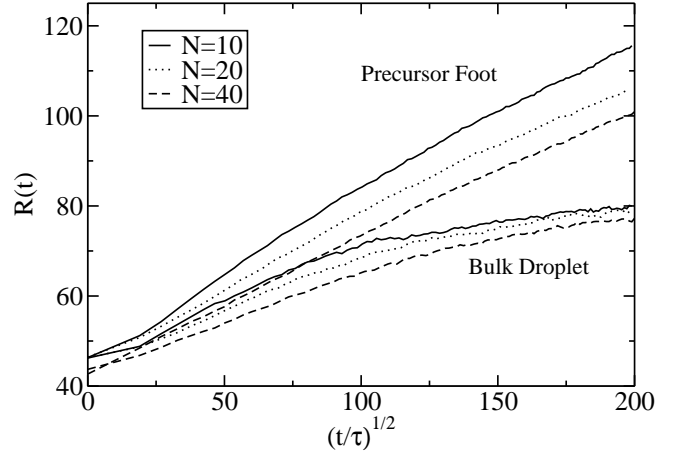


FIG. 8: Chain length dependence of the contact radius of the precursor foot and bulk droplet for wetting droplets on a flat surface with  $\varepsilon_w = 2.0 \varepsilon$ . The surface Langevin thermostat is applied with  $\gamma_L^s = 10.0 \tau^{-1}$ .

The molecular kinetic theory of liquids developed by Eyring and coworkers [19] has been applied to droplet spreading by Blake and Haynes [21]. It focuses on the adsorption of liquid molecules to the surface as the dominant factor in energy dissipation. In this theory, the liquid molecules jump between surface sites separated by a distance  $\lambda$  with a frequency  $K$ . The velocity of the contact line is related to the contact angle  $\theta$  by

$$\frac{dR}{dt} = 2K\lambda \sinh \left[ \left( \frac{\gamma}{2\Delta n k_B T} \right) (\cos \theta - \cos \theta_0) \right] \quad (13)$$

where  $\gamma$  is the surface tension of the liquid/vapor interface,  $\Delta n$  is the density of sites on the solid surface, and  $\theta_0$  is the equilibrium contact angle. For sufficiently low velocities, the equation can be written in its linearized form,

$$\frac{dR}{dt} = \frac{K\lambda\gamma}{\Delta n k_B T} (\cos \theta_0 - \cos \theta). \quad (14)$$

Assuming the droplet maintains constant volume and the shape of a spherical cap, the velocity of the contact line can be expressed in terms of the time dependence of the contact angle purely from geometric arguments giving

$$\frac{dR}{dt} = - \left( \frac{3V}{\pi} \right)^{1/3} \frac{(1 - \cos \theta)^2}{(2 - 3 \cos \theta + \cos^3 \theta)^{4/3}} \frac{d\theta}{dt}. \quad (15)$$

Combining Eqs. 14 and 15 gives an expression for the time dependence of the contact angle,

$$\frac{d\theta}{dt} = - \left( \frac{\pi}{3V} \right)^{1/3} \Omega(\theta) \frac{\gamma}{\zeta_0} (\cos \theta_0 - \cos \theta) \quad (16)$$

where

$$\Omega(\theta) = \frac{(2 - 3 \cos \theta + \cos^3 \theta)^{4/3}}{(1 - \cos \theta)^2} \quad (17)$$

and  $\zeta_0$  is the friction coefficient defined as  $\zeta_0 = \frac{\Delta n k_B T}{K \lambda}$ , which has units of viscosity.

The hydrodynamic model [24] describes the flow pattern that forms in the bulk of the droplet as material is transferred to the advancing contact line. This model can be obtained by solving the equations of motion and continuity for the droplet described as a cylindrical disk [51] instead of a spherical cap. Neglecting the flow perpendicular to the surface and balancing the radial shear stress at the top of the cylinder with the effective radial surface tension, the velocity of the contact line is written as

$$\frac{dR}{dt} = \frac{4\gamma V^3}{\pi^3 \eta R^9} - \frac{\gamma \beta V}{2\pi \eta R^3} \quad (18)$$

where  $V$  is the droplet volume,  $\eta$  is the viscosity of the liquid, and  $\beta = 1 - \cos \theta_0$ . Equation 18 is in agreement with Tanner's spreading law [2] for completely wetting systems ( $\theta_0 = 0$ ) and for non-wetting systems with small equilibrium contact angles, giving  $R \sim t^{1/10}$  at long times. Instead of directly combining Eqs. 15 and 18, we apply the approach of de Ruijter *et al.* [8, 10] in order to make a direct comparison with the combined model presented below. Using the same cylindrical disk model, they neglect the flow perpendicular to the surface and specify that the velocity at the upper edge of the cylinder is the actual droplet spreading rate,  $dR/dt$ . With this approach, they find that the hydrodynamic dissipation term can be written as

$$T \sum_w = 6\pi R(t) \eta \phi[\theta(t)] \left( \frac{dR}{dt} \right)^2 \ln [R(t)/a] \quad (19)$$

where  $\phi(\theta)$  is a geometric factor defined as

$$\phi(\theta) = \frac{\sin^3 \theta}{2 - 3 \cos \theta + \cos^3 \theta} \quad (20)$$

and  $a$  is an adjustable parameter that represents the radius of the core region of the droplet, where the radial flow is negligible. For the hydrodynamic model, they obtain

$$\frac{d\theta}{dt} = - \left( \frac{\pi}{3V} \right)^{1/3} \Omega(\theta) \frac{\gamma (\cos \theta_0 - \cos \theta)}{6\eta \phi(\theta) \ln [R/a]}. \quad (21)$$

Both types of dissipation are present in the spreading droplet. The hydrodynamic mechanism is expected to dominate at low velocities and small contact angles while the kinetic mechanism is expected to dominate at high velocities and large contact angles [25]. We include in our comparison a model developed by de Ruijter *et al.* [8, 10] containing both kinetic and hydrodynamic terms. In this model, the velocity of the contact line is written as

$$\frac{dR}{dt} = \frac{\gamma [\cos \theta_0 - \cos \theta]}{\zeta_0 + 6\eta \phi(\theta) \ln [R/a]}. \quad (22)$$

TABLE I: Bulk properties of bead-spring chains obtained from MD simulation for  $T = \varepsilon/k_B$ ,  $P \simeq 0$ .

N	$\rho$ ( $\sigma^{-3}$ )	$\gamma$ ( $\varepsilon/\sigma^2$ )	$\eta$ (m/ $\tau\sigma$ )	$10^3 D$ ( $\sigma^2/\tau$ )	$\zeta_R$ ( $\tau^{-1}$ )
10	0.8691	$0.85 \pm 0.02$	$11.1 \pm 0.4$	$6.17 \pm 0.06$	16.2
20	0.8803	$0.92 \pm 0.02$	$17.4 \pm 0.7$	$3.04 \pm 0.03$	16.4
40	0.8856	$0.95 \pm 0.02$	$41.7 \pm 1.4$	$1.23 \pm 0.01$	20.4

Combining this with Eq. 15 gives

$$\frac{d\theta}{dt} = - \left( \frac{\pi}{3V} \right)^{1/3} \Omega(\theta) \frac{\gamma (\cos \theta_0 - \cos \theta)}{\zeta_0 + 6\eta \phi(\theta) \ln [R/a]}. \quad (23)$$

## B. Analysis of Models

Fitting simulation data to the models described above requires both the liquid/vapor surface tension and the bulk viscosity of the polymer. The surface tension,  $\gamma$ , is obtained by first constructing a slab of the polymer melt containing 10,000 chains of  $N = 10$ , 5000 chains of  $N = 20$ , or 5000 chains of  $N = 40$  centered in the simulation box such that there are two surfaces perpendicular to the  $z$  direction. The simulations are run at temperature  $T = 1.0$  and pressure  $P \simeq 0$  without tail corrections. We leave out tail corrections to the pressure in order to match the system of the spreading droplet. The simulations are run until the two liquid/vapor interfaces are equilibrated, as determined by the density profiles across the interfaces. From the equilibrium values of the pressure, parallel and perpendicular to the interfaces,  $\gamma$  can easily be determined from [52]

$$\gamma = \frac{1}{2} \int_0^{L_z} [p_{\perp}(z) - p_{\parallel}(z)] dz. \quad (24)$$

The values for the surface tension are summarized in Table I. These values can be compared to  $\gamma = 0.08 \varepsilon/\sigma^2$  for a system of monomers [53].

The viscosity is computed from the equilibrium fluctuations of the off-diagonal components of the pressure tensor [54]. The pressure tensors are recorded from simulations of systems containing melts of 500 chains of the  $N = 10$  polymer, 250 chains of the  $N = 20$  polymer, and 500 chains of the  $N = 40$  polymer at  $T = 1.0$  with the bulk pressure  $P \simeq 0$  without tail corrections. These simulations are run at a timestep  $\Delta t = 0.006$  for up to 25,000  $\tau$ . The autocorrelation function of each off-diagonal component of the stress tensor is calculated using the Numerical Recipes routine CORREL [55]. The autocorrelation functions are averaged to improve statistical uncertainty. From this, the viscosity can be calculated using [54]

$$\eta = \frac{V}{k_B T} \int_0^\infty dt \langle \sigma_{\alpha\beta}(t) \sigma_{\alpha\beta}(0) \rangle. \quad (25)$$

The results for  $\eta$  are summarized in Table I.

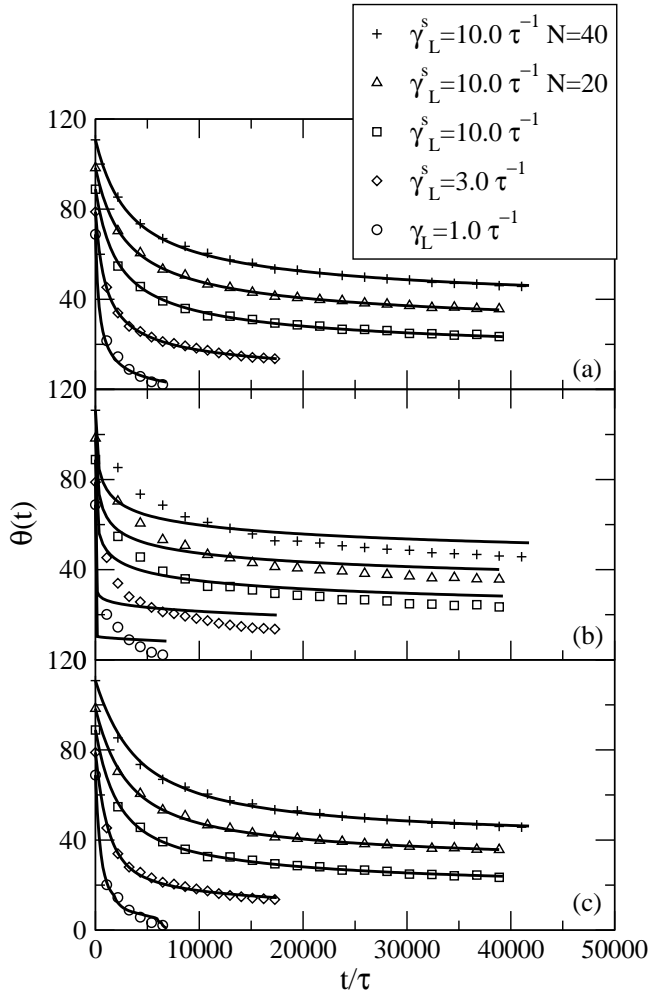


FIG. 9: Fits to contact angle data (symbols) of (a) kinetic, (b) hydrodynamic and (c) combined models for wetting droplets on a flat surface with  $\varepsilon_w = 2.0 \varepsilon$ . The chain length is  $N = 10$  unless otherwise specified. The Langevin thermostat is applied to all monomers ( $\gamma_L$ ) or just monomers near the surface ( $\gamma_L^s$ ). The data sets are shifted by  $10^\circ$  increments (except for  $\gamma_L^s = 1.0 \tau^{-1}$ ) for clarity.

Estimates of the friction coefficients,  $\zeta_R$ , obtained from the melt simulations, are included in Table I. The diffusion constant  $D$  is determined from the mean square displacement of the middle monomers of each chain and using the Rouse model one can extract  $\zeta_R$  from  $D = \frac{k_B T}{m N \zeta_R}$  [56].

With the above values for the surface tension and viscosity, the simulation data is fit to each of the models described above. The fit is performed by taking initial guess values for the independent parameters and integrating the expression for  $d\theta/dt$  defined in one of the equations 16, 21, or 23. The integration uses the fourth-order Runge-Kutta method to generate a set of data,  $\theta_{calc}(t)$ . The parameters are varied using the downhill simplex method [55] until the difference between the model and simulation data,  $|\theta_{calc}(t) - \theta(t)| / \theta(t)$ , is minimized.

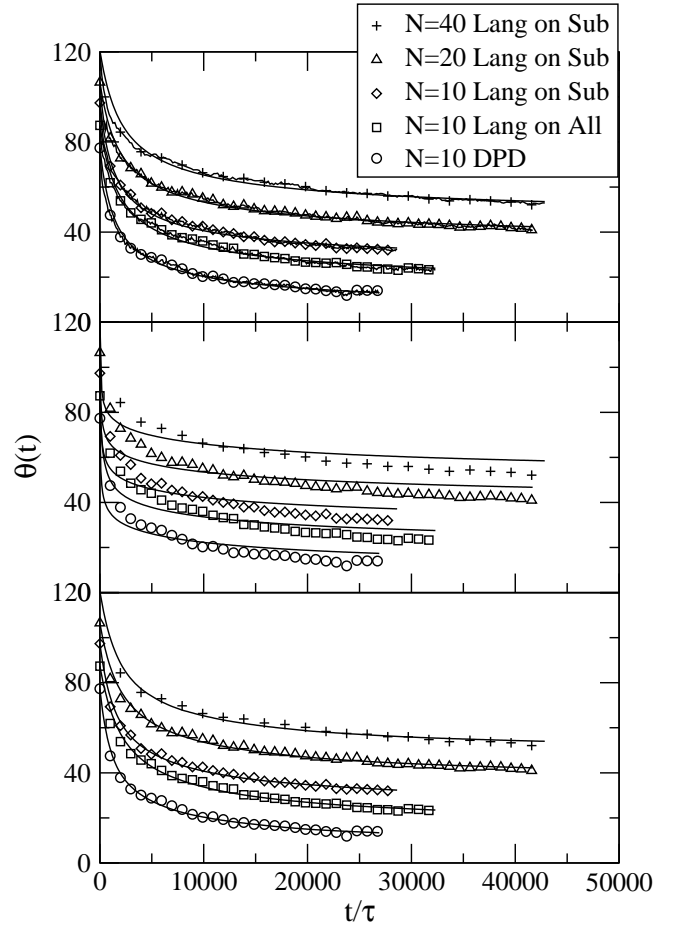


FIG. 10: Fits to contact angle data (symbols) of (a) kinetic, (b) hydrodynamic and (c) combined models for wetting droplets on the medium atomistic substrate with  $\varepsilon_{12} = 1.5 \varepsilon$ . The Langevin thermostat is applied to all monomers or to just substrate monomers.  $\gamma_L = 0.1 \tau^{-1}$  for all cases except DPD where  $\gamma_{DPD} = 0.1 \tau^{-1}$ . The data sets are shifted by  $10^\circ$  increments (except for  $N = 10$  DPD) for clarity.

The kinetic, hydrodynamic and combined models are fit to the contact angles of droplets spreading on a flat surface in Fig. 9. The Langevin thermostat is applied either to all monomers or only to those near the surface. We find that both the kinetic and combined models fit the data well despite the fact that they predict that the friction coefficient,  $\zeta_0$ , is larger in the combined model than in the kinetic model. The hydrodynamic model produces a very poor fit to each data set as shown in Fig. 9b. The best fit parameters for these models applied to data for wetting droplets on a flat surface are shown in Table II. The error reported for each model is calculated as

$$\chi^2 = \frac{1}{\mathcal{N}} \sum_{i=1}^{\mathcal{N}} \frac{|\theta_{calc}(t) - \theta(t)|^2}{\theta(t)} \quad (26)$$

where  $\mathcal{N}$  is the number of data points in each set of data.

Figure 10 shows the kinetic, hydrodynamic, and combined model fits to the contact angle data for wetting



TABLE II: Model parameters and error estimates resulting from fits to contact angle data from simulations of wetting droplets on a flat surface. Values for  $\gamma_L$  and  $\gamma_L^s$  are listed in the first column.  $\varepsilon_w = 2.0 \varepsilon$ .

Thermostat	N	Kinetic $\zeta_0 \left( \frac{m}{\tau \sigma} \right)$	Hydrodynamic $a(\sigma)$	Combined $\zeta_0 \left( \frac{m}{\tau \sigma} \right) \quad a(\sigma)$		$\chi_{kin}^2$	$\chi_{hydro}^2$	$\chi_{comb}^2$
$\gamma_L = 1.0 \tau^{-1}$	10	9.55	44.40	35.41	71.23	0.0022	0.047	0.0039
$\gamma_L^s = 3.0 \tau^{-1}$	10	25.97	42.29	57.27	71.55	0.00028	0.025	0.0011
$\gamma_L^s = 10.0 \tau^{-1}$	10	56.30	38.14	89.98	83.80	0.00024	0.018	0.00028
$\gamma_L^s = 10.0 \tau^{-1}$	20	81.37	38.83	137.99	84.77	0.00015	0.015	0.00023
$\gamma_L^s = 10.0 \tau^{-1}$	40	101.29	38.63	200.45	86.49	0.00022	0.024	0.00036

droplets on the medium substrate. Again, the hydrodynamic model gives a significantly worse fit to the data. The best fit parameters for these models for wetting droplets on an atomistic substrate are shown in Table III. The kinetic and combined models give friction coefficients that are generally larger than the bulk viscosity for the range of coupling parameters used here. We find that, in contrast with previous work by De Ruijter *et al.* [8, 10], the combined model predicts a larger friction coefficient than the kinetic model. Also, the hydrodynamic and combined models give a value of  $a$  that is on the order of the radius of the droplet, indicating that hydrodynamic flow is not a dominant feature of the spreading of these droplets, at least for the time scales accessible to simulation.

## V. CONCLUSIONS

In this study, we perform molecular dynamics simulations of polymer droplets that are roughly an order of magnitude greater in size than those previously studied. We find this to be necessary to adequately model the behavior of the precursor foot and the bulk material simultaneously. Starting from a hemispherical droplet, we find that the precursor foot forms immediately and spreads diffusively for each system where the surface interaction strength is above the wetting/non-wetting transition. The bulk region of the droplet spreads at a significantly slower rate, but the data is too imprecise to distinguish between, for example, a  $t^{1/7}$  or a  $t^{1/10}$  scaling.

We perform spreading simulations on both an atomistically realistic substrate and a perfectly flat surface. The simulations using a flat surface exhibit the same behavior as the realistic substrate and greatly improve the computational efficiency since the number of monomers on the realistic substrate is typically several times greater than the number of monomers in the droplet. However, to do so, it is critical to apply a thermostat that couples only to monomers near the surface. On an atomistic substrate, the most efficient method is to couple only the substrate particles to the thermostat. This is computationally faster than coupling all monomers to the DPD thermostat and leads to the same results.

Several droplet spreading models have been developed to fit contact angle data. A simple kinetic mechanism for energy dissipation fits the data well and provides rea-

sonable values for the friction coefficients, which we verified through separate polymer melt simulations. Using a combined model that adds a hydrodynamic energy dissipation mechanism slightly improves the fit, but resulted in less accurate estimates of the friction coefficients. The fact that we do not observe evidence of hydrodynamic flow behavior may be due to the small droplet sizes accessible to molecular dynamics simulation. Evidence for hydrodynamic effects on spreading has been observed experimentally for macroscopic drops [2, 12, 57]. The length scale where hydrodynamic effects become important remains an open question.

Future work will include studying the spreading behavior of binary droplets and developing more realistic surface interactions.

## VI. ACKNOWLEDGEMENTS

We thank M. O. Robbins for helpful discussions. Sandia is a multiprogram laboratory operated by Sandia Corporation, a Lockheed Martin Company, for the United States Department of Energy's National Nuclear Security Administration under Contract No. DE-AC04-94AL85000.

TABLE III:

Model parameters and error estimates resulting from fits to contact angle data from simulations of wetting droplets on an atomistic substrate.  $\varepsilon_{12} = 1.5 \varepsilon$ ,  $\gamma_{DPD} = \gamma_L = 0.1 \tau^{-1}$ .

Thermostat	N	Kinetic $\zeta_0 \left( \frac{m}{\tau} \right)$	Hydrodynamic $a(\sigma)$	Combined		$\chi_{kin}^2$	$\chi_{hydro}^2$	$\chi_{comb}^2$
DPD	10	36.7	42.1	53.4	65.5	0.001	0.015	0.001
Lang on All	10	50.8	38.1	81.8	70.0	0.001	0.015	0.001
Lang on Sub	10	38.0	41.8	64.9	69.6	0.001	0.020	0.001
Lang on Sub	20	54.4	43.2	91.9	68.3	0.001	0.020	0.001
Lang on Sub	40	65.5	42.9	126	64.0	0.002	0.019	0.002

- 
- [1] C. Huh and L. E. Scriven, *J. Coll. Interface Sci.* **35**, 85 (1971).
- [2] L. H. Tanner, *J. Phys. D* **12**, 1473 (1979).
- [3] P. G. de Gennes, *Rev. Mod. Phys.* **57**, 827 (1985).
- [4] F. Heslot, N. Fraysse, and A. M. Cazabat, *Nature* **338**, 640 (1989).
- [5] M. J. de Ruijter, J. De Coninck, T. D. Blake, A. Clarke, and A. Rankin, *Langmuir* **13**, 7293 (1997).
- [6] M. Voué, M. P. Valignat, G. Oshanin, A. M. Cazabat, and J. De Coninck, *Langmuir* **14**, 5951 (1998).
- [7] S. Gerdes, A. M. Cazabat, G. Ström, and F. Tiberg, *Langmuir* **14**, 7052 (1998).
- [8] M. J. de Ruijter, J. De Coninck, and G. Oshanin, *Langmuir* **15**, 2209 (1999).
- [9] S. Semal, T. D. Blake, V. Geskin, M. J. de Ruijter, G. Castelein, and J. De Coninck, *Langmuir* **15**, 8765 (1999).
- [10] M. J. de Ruijter, M. Charlot, M. Voué, and J. De Coninck, *Langmuir* **16**, 2363 (2000).
- [11] M. Voué and J. De Coninck, *Acta Materialia* **48**, 4405 (2000).
- [12] E. Pérez, E. Schäffer, and U. Steiner, *J. Coll. Interface Sci.* **234**, 178 (2001).
- [13] T. D. Blake and Y. D. Shikhmurzaev, *J. Coll. Interface Sci.* **253**, 196 (2002).
- [14] M. Cachile, O. Bénichou, and A. M. Cazabat, *Langmuir* **18**, 7985 (2002).
- [15] M. Cachile, O. Bénichou, C. Poulard, and A. M. Cazabat, *Langmuir* **18**, 8070 (2002).
- [16] F. Heslot, A. M. Cazabat, P. Levinson, and N. Fraysse, *Phys. Rev. Lett.* **65**, 599 (1990).
- [17] N. Fraysse, M. P. Valignat, A. M. Cazabat, F. Heslot, and P. Levinson, *J. Coll. Interface Sci.* **158**, 27 (1993).
- [18] V. E. Dussan and S. Davis, *J. Fluid Mech.* **65**, 71 (1974).
- [19] S. Gladstone, K. J. Laidler, and H. J. Eyring, *The Theory of Rate Processes* (McGraw-Hill, New York, 1941).
- [20] T. D. Blake, *The Contact Angle and Two-phase Flow* (Ph.D. Thesis, University of Bristol, 1968).
- [21] T. D. Blake and J. M. Haynes, *J. Coll. Interface Sci.* **30**, 421 (1969).
- [22] B. W. Cherry and C. M. Holmes, *J. Coll. Interface Sci.* **29**, 174 (1969).
- [23] O. V. Voinov, *Fluid Dynamics* **11**, 714 (1976).
- [24] R. G. Cox, *J. Fluid Mech.* **168**, 169 (1986).
- [25] F. Brochard-Wyart and P. G. de Gennes, *Adv. Coll. Interface Sci.* **39**, 1 (1992).
- [26] P. G. de Gennes, *Liquids at Interfaces* (North-Holland, New York, 1990), p. 371.
- [27] P. G. Petrov and J. G. Petrov, *Langmuir* **8**, 1762 (1992).
- [28] T. D. Blake, *Wettability* (Marcel Dekker, New York, 1993).
- [29] J. Yang, J. Koplik, and J. R. Banavar, *Phys. Rev. Lett.* **67**, 3539 (1991).
- [30] J. Yang, J. Koplik, and J. R. Banavar, *Phys. Rev. A* **46**, 7738 (1992).
- [31] S. M. Thompson, K. E. Gubbins, J. P. R. B. Walton, R. A. R. Chantry, and J. S. Rowlinson, *J. Chem. Phys.* **81**, 1 (1984).
- [32] P. van Remoortere, J. E. Metrz, L. E. Scriven, and H. T. David, *J. Chem. Phys.* **110**, 2621 (1999).
- [33] J. De Coninck, U. D'Ortona, J. Koplik, and J. R. Banavar, *Phys. Rev. Lett.* **74**, 928 (1995).
- [34] U. D'Ortona, J. De Coninck, J. Koplik, and J. R. Banavar, *Phys. Rev. E* **53**, 562 (1996).
- [35] X. Wu, N. Phan-Thien, X. Fan, and T. Y. Ng, *Phys. Fluids* **15**, 1357 (2003).
- [36] J. A. Nieminen, D. B. Abraham, M. Karttunen, and K. Kaski, *Phys. Rev. Lett.* **69**, 124 (1992).
- [37] J. A. Nieminen and T. Ala-Nissila, *Phys. Rev. E* **49**, 4228 (1994).
- [38] S. Bekink, S. Karaborni, G. Verbist, and K. Esselink, *Phys. Rev. Lett.* **76**, 3766 (1996).
- [39] A. Milchev and K. Binder, *J. Chem. Phys.* **116**, 7691 (2002).
- [40] T. D. Blake, A. Clarke, J. De Coninck, and M. J. de Ruijter, *Langmuir* **13**, 2164 (1997).
- [41] M. J. de Ruijter, T. D. Blake, and J. De Coninck, *Langmuir* **15**, 7836 (1999).
- [42] T. D. Blake, A. Clarke, J. De Coninck, M. de Ruijter, and M. Voué, *Colloids and Surfaces A* **149**, 123 (1999).
- [43] M. de Ruijter, T. D. Blake, A. Clarke, and J. De Coninck, *J. Petroleum Science Eng.* **24**, 189 (1999).
- [44] F. Heslot, A. M. Cazabat, and P. Levinson, *Phys. Rev. Lett.* **62**, 1286 (1989).
- [45] O. M. Braun and M. Peyrand, *Phys. Rev. E* **63**, 046110 (2001).
- [46] K. Kremer and G. S. Grest, *J. Chem. Phys.* **92**, 5057 (1990).
- [47] S. Plimpton, *J. Comput. Phys.* **117**, 1 (1995).
- [48] G. S. Grest and K. Kremer, *Phys. Rev. A* **33**, 3628 (1986).
- [49] P. J. Hoogerbrugge and J. M. V. A. Koelman, *Europhys. Lett.* **19**, 155 (1992).
- [50] P. Español and P. Warren, *Europhys. Lett.* **30**, 191 (1995).
- [51] A. E. Seaver and J. G. Berg, *J. App. Poly. Sci.* **52**, 431

- (1994).
- [52] M. J. P. Nijmeijer, A. F. Bakker, C. Bruin, and J. H. Sikkenk, J. Chem. Phys. **89**, 3789 (1988).
  - [53] S. W. Sides, G. S. Grest, and M.-D. Lacasse, Phys. Rev. E **60**, 6708 (1999).
  - [54] M. Allen and D. Tildesley, *Computer Simulation of Liquids* (Clarendon Press, Oxford, 1987).
  - [55] W. H. Press, S. A. Teukolsky, W. T. Vetterling, and B. P. Flannery, *Numerical Recipes in C* (Cambridge University Press, Cambridge, 1992).
  - [56] M. Doi and S. F. Edwards, *The Theory of Polymer Dynamics* (Clarendon Press, Oxford, 1986).
  - [57] G. Garnier, M. Bertin, and M. Smrckova, Langmuir **15**, 7863 (1999).